



Numerical simulation of steady-state thermal blooming with natural convection

JEREMIAH S. LANE,^{1,*}  JUSTIN COOK,² MARTIN RICHARDSON,² AND BENJAMIN F. AKERS¹

¹Department of Mathematics and Statistics, Air Force Institute of Technology, Wright-Patterson AFB, Ohio, 45433, USA

²Laser Plasma Laboratory, CREOL, the College of Optics & Photonics, University of Central Florida, Orlando, Florida, 32816, USA

*jeremiah.lane@afit.edu

Received 22 December 2022; revised 6 February 2023; accepted 8 February 2023; posted 9 February 2023; published 7 March 2023

This work investigates steady-state thermal blooming of a high-energy laser in the presence of laser-driven convection. While thermal blooming has historically been simulated with prescribed fluid velocities, the model introduced here solves for the fluid dynamics along the propagation path using a Boussinesq approximation to the incompressible Navier–Stokes equations. The resultant temperature fluctuations were coupled to refractive index fluctuations, and the beam propagation was modeled using the paraxial wave equation. Fixed-point methods were used to solve the fluid equations as well as to couple the beam propagation to the steady-state flow. The simulated results are discussed relative to recent experimental thermal blooming results [Opt. Laser Technol. 146, 107568 (2022)], with half-moon irradiance patterns matching for a laser wavelength at moderate absorption. Higher energy lasers were simulated within an atmospheric transmission window, with the laser irradiance exhibiting crescent profiles. © 2023 Optica Publishing Group

<https://doi.org/10.1364/AO.484224>

1. INTRODUCTION

This paper considers the steady-state propagation of a CW laser in the presence of thermal blooming. Historically, simulations of thermal blooming have relied on prescriptions of the fluid velocity through scaling laws or statistical measures [1–3]. While useful in capturing the magnitude of velocity, especially in the presence of significant wind, these simulations fail to capture the nonlinear fluid dynamics associated with buoyancy-driven convection caused by energy absorption from the laser [4–6]. In an effort to account for the nonlinearity in the flow, we solve for the flow velocity directly through a buoyancy-driven approximation to the Navier–Stokes equations.

The phenomenon of thermal blooming is a physical process that is often detrimental to the performance of laser beam propagation. The present literature reflects an increasing interest in understanding this effect, with recent efforts devoted to numerical simulations with more comprehensive physical processes [4,7–9]. Specifically, much of the contemporary research has focused on the mechanics of laser-induced convection, high-energy laser propagation, and propagation through atmospheric aerosols [2,10,11]. This knowledge can then be applied in laser holography [12] and in the development of adaptive optics systems [13–15].

The research of atmospheric laser propagation has been developed alongside laser technology since applications involving lasers were first introduced in the 1960s [16]. With improving technology, the breadth of applications for laser propagation has especially expanded since the turn of the century [17,18]. CW

lasers can now output power in the kilowatt regime, a threshold sure to increase with time. The present use of high energy lasers is diverse, with applications in both the civil and defense spheres. Applications include climate prediction and weather control [19], measurement and wave mixing in nanofluids [20,21], microparticle manipulation [22,23], ground vehicle-deployable weapons systems [24], material testing of hypersonic flight conditions [25], and rapid charging of in-flight unmanned aerial vehicles [26]. As part of a comprehensive model for laser beam propagation through a medium with an inhomogeneous index of refraction, it is necessary to consider the cumulative effects of molecular and aerosol absorption of beam energy [11,27,28]. In the Boussinesq approximation, this absorption creates temperature fluctuations in the fluid, which drives the buoyancy-driven fluid dynamics through natural convection. As the laser propagates through the fluid, the energy loss due to absorption combines with the beam intensity losses due to scattering, the sum of which is the attenuation (extinction) coefficient in the beam evolution equation. The absorption and attenuation coefficients can vary significantly depending on factors such as atmospheric aerosol content or whether the laser wavelength lies within a water absorption band [28,29]. To see fully formed crescent or half-moon shapes in irradiance that are characteristic of strong thermal blooming, there must be a high degree of laser energy absorbed into the propagating medium. In Section 2, we discuss how this manifests through the nondimensional Stanton (St) number with commentary on specific regimes where strong thermal blooming may be seen.

A majority of the efforts to simulate thermal blooming have been devoted to the time-dependent regime, where the steady-state flow may be reached after a sufficient time has passed. In applications involving time scales that exceed the time-dependent dynamics of thermal blooming, however, it is advantageous to solve for steady-state solutions directly if they are accessible. In a previous work, the authors [30] developed a numerical method to solve for the 2D steady-state in fluid flows, with a proof of existence and uniqueness for a small enough laser absorption factor. The method uses fast Poisson equation solvers on a finite difference grid, allowing for fast performance in computing the fluid steady state. The fluid dynamics are coupled to the beam using a steady version of the Akers and Reeger model [4].

This work focuses exclusively on the effect of thermal blooming in the natural convection regime, so no scintillation or background wind is simulated. Aerosol effects are assumed to be captured entirely within the absorption and scattering coefficients. Sprangle *et al.* [11,28] provides an analysis of laser beam degradation due to different molecular and aerosol absorption and scattering coefficients. The results of the simulation are discussed as it compares to recent experimental work [31].

This article has four sections. Section 2 describes in detail the assumptions and methods used in the steady-state simulations, along with the methodology applied in choosing specific simulation parameters. Section 3 follows with the results of the simulations and offers a discussion on the takeaways from the results. Section 4 summarizes the article and presents future research areas to build off of the contributions contained here.

2. FORMULATION

This section describes the mathematical models and tools used to simulate steady-state thermal blooming. The equations include the paraxial equation for beam evolution and the Navier–Stokes equations for fluid velocity and temperature. The numerical methods are developed for the computation of 2D steady states in the fluid and the calculation of the coupled laser intensity with the fluid dynamics.

A. Physical Models

We seek to model the propagation of a CW laser with known properties and a prescribed irradiance profile at the aperture. The laser propagates a specified distance through a 3D, steady atmosphere. The variables of interest are the beam intensity along the propagation path as well as the fluid temperature and velocity. There are two distinct distance scales that dictate the behavior of the coupled laser and fluid. The first scale exists in the transverse (x, y) plane and is associated with the size in which the beam spreads, often on the order of single centimeters. The second scale is defined by the distance in which the laser propagates in the z direction, which for atmospheric applications is on the order of meters to kilometers. This separation of scales forms the basis for the use of the paraxial approximation for laser evolution. Within this paraxial scaling, the fluid flow is 2D to the same order of accuracy as the laser evolution, as argued in Akers and Reeger [4].

From this separation of scales, we seek the steady-state fluid properties within a 2D domain that represents a rectangular cross section along the z path of the laser beam. The atmosphere is assumed to be an incompressible, Newtonian fluid that is governed by the Boussinesq approximation for buoyancy-driven flows. The Boussinesq model is accurate for flows in which temperature differences exclusively drive motion under the influence of gravity [32]. The variations in fluid density are related to variations in temperature through the ideal gas relation

$$\frac{\rho_1}{\rho_0} = \frac{\tau_1}{\tau_0}, \tag{1}$$

where ρ_1 is a fluctuation about a mean density ρ_0 and τ_1 is a fluctuation about a reference temperature τ_0 . The nondimensional steady-state Navier–Stokes equations in the Boussinesq approximation are given by

$$(\mathbf{u} \cdot \nabla)\mathbf{u} = -\nabla p + \frac{1}{\text{Re}}\nabla^2\mathbf{u} + \text{Ri}T\mathbf{e}_2, \tag{2a}$$

$$\nabla \cdot \mathbf{u} = 0, \tag{2b}$$

$$(\mathbf{u} \cdot \nabla)T = \frac{1}{\text{Pe}}\nabla^2 T + \text{St}|V|^2. \tag{2c}$$

Here, the velocity $\mathbf{u} = (u, v, 0)$ is 2D and the temperature $T = \frac{\tau_1}{\tau_0}$ is the normalized temperature fluctuation. The term $|V|^2$ again represents the laser forcing term, $\mathbf{e}_2 = (0, 1)$ is the unit vector in the vertical (y) direction, and p is the nondimensional pressure scaled by $p_0 = \rho_0 U^2$. The parameters in the nondimensionalization in Eq. (2) are the Reynolds (Re), Peclet (Pe), Richardson (Ri), and St numbers, which are defined as

$$\text{Re} = \frac{UL_x}{\nu}, \quad \text{Pe} = \frac{UL_x}{\mu}, \quad \text{Ri} = \frac{gL_x}{U^2}, \quad \text{St} = \frac{\beta V_0^2 L_x}{U\tau_0}. \tag{3}$$

These definitions contain a length scale L_x , a characteristic velocity scale U , acceleration due to gravity g , kinematic viscosity ν , thermal diffusivity μ , temperature scale τ_0 , laser absorption coefficient β , and peak laser intensity V_0^2 . This method of nondimensionalization differs from other common approaches for natural convection problems [33]; however, it is useful in that it facilitates direct comparison to other convection studies with a prescribed characteristic velocity. Since the degree of convection in this problem depends on the energy injection from the laser, there is no immediate choice for U . The appropriate velocity scale is thus determined *a posteriori* based on the peak vertical velocity in the steady solution. The steady flow solutions are invariant to this velocity scale, so the choice for U is arbitrary. For all simulations, we initially choose $U = 1$ cm/s and report the updated parameters based on the computed velocity scale. The Ri number represents the contribution of gravity to the flow through the buoyancy mechanism. The St number measures the interaction between the laser with the fluid as a ratio of heat taken in by the fluid through absorption and convective heat transfer throughout the rest of the domain. Greater peak intensity and stronger fluid absorption thus correspond to higher Stanton numbers.

In 2D, it is useful to solve the fluid equations in Eq. (2) in the streamfunction-vorticity form [34]

$$(\mathbf{u} \cdot \nabla) T = \frac{1}{\text{Pe}} \nabla^2 T + \text{St} |V|^2, \quad (4a)$$

$$(\mathbf{u} \cdot \nabla) \omega = \frac{1}{\text{Re}} \nabla^2 \omega + \text{Ri} \partial_x T, \quad (4b)$$

$$\nabla^2 \psi = -\omega, \quad (4c)$$

$$u = \partial_y \psi, \quad (4d)$$

$$v = -\partial_x \psi, \quad (4e)$$

where $\omega = \partial_x v - \partial_y u$ is the vorticity and ψ is the streamfunction of the fluid. The system enforces incompressibility by definition. This ameliorates difficulties in applying a pressure correction scheme to ensure divergence-free flow in steady solutions while using primitive variables [35].

The paraxial equation for the complex beam amplitude V in dimensionless units [11] is

$$\frac{\partial V}{\partial z} = \left(\frac{i}{2n_0 F} \nabla_{\perp}^2 - i L_z n_1 k - L_z (\alpha_f + \alpha_a) \right) V, \quad (5)$$

where

$$F = \frac{L_x^2 k}{L_z} \quad (6)$$

is the Fresnel number [1,2], L_z is the propagation distance, L_x is the beam radius and the length scale of the flow, ∇_{\perp}^2 is the Laplacian in the transverse (x, y) plane, k is the laser wavenumber, n_0 is the ambient refractive index, n_1 is a fluctuation in the refractive index, α_f is the extinction coefficient due to the fluid, and α_a is the extinction coefficient due to aerosols. Each simulated propagation distance is such that the Fresnel number F is of order unity. Each extinction coefficient is the sum of beam energy loss due to absorption and scattering. The refractive index fluctuation is linearly coupled to density fluctuations through the Gladstone–Dale relationship [36]

$$n_1 = (n_0 - 1) \frac{\rho_1}{\rho_0}, \quad (7)$$

from which the ideal gas relation in Eq. (1) results in the following relationship between temperature fluctuations and refractive index fluctuations:

$$n_1 = (n_0 - 1) \frac{\tau_1}{\tau_0}. \quad (8)$$

The solution to the paraxial equation describes the propagation of the laser beam in space as a function of the variation in the index of refraction, the extinction from aerosols, and the extinction from the surrounding fluid. This formulation introduces the nonlinear coupling between the equations governing the behavior of the laser and the fluid. We emphasize here that this study focuses strictly on the steady-state flow. The following subsection discusses the fixed-point approach used to arrive

at the steady-state flow solution; however, there may be other steady states in the flow that the method fails to compute. The fixed-point method discussed here guarantees the existence and uniqueness of steady solutions for a sufficiently small St number [30], but gives no insight into other steady-state flow solutions for larger St numbers or those that deviate significantly from a quiescent fluid. Generally, the observed steady state depends on the precise initial conditions of the physical scenario. Thus, in a lab setting, the experimental flow may reach a different steady state to the one predicted in the simulations. Further work in simulating large St number steady blooming must consider multiple steady states and their stability.

B. Simulation Methods

1. Fluid Solver

The approach to solving for the fluid steady-state is as follows. Given a normalized laser irradiance profile $|V(x, y, z_j)|^2$, we solve the steady-state Boussinesq equations in Eqs. (4a)–(4e) in streamfunction-vorticity form over a rectangular domain corresponding to a transverse slice at the longitudinal distance z_j . We consider a slip boundary condition on a finite box corresponding to zero shear stress along the boundary where the normal component of velocity at the boundary vanishes but the tangential component is unrestricted. The temperature fluctuation is assumed to be zero along the boundary. We employed the fixed-point method introduced in [30] that uses discrete Poisson equation solvers to converge to the steady-state solution. The iteration for $n \geq 1$ is

$$\nabla^2 T_n = \text{Pe} \left(\frac{\partial \psi_{n-1}}{\partial y} \frac{\partial T_{n-1}}{\partial x} - \frac{\partial \psi_{n-1}}{\partial x} \frac{\partial T_{n-1}}{\partial y} - \text{St} |V|^2 \right), \quad (9a)$$

$$\nabla^2 \omega_n = \text{Re} \left(\frac{\partial \psi_{n-1}}{\partial y} \frac{\partial \omega_{n-1}}{\partial x} - \frac{\partial \psi_{n-1}}{\partial x} \frac{\partial \omega_{n-1}}{\partial y} - \text{Ri} \frac{\partial T_n}{\partial x} \right), \quad (9b)$$

$$\nabla^2 \psi_n = -\omega_n, \quad (9c)$$

where the algorithm is initialized by the linearization

$$\nabla^2 T_0 = -\text{Pe} (\text{St} |V|^2), \quad (10a)$$

$$\nabla^2 \omega_0 = -\text{Ri} \text{Re} \frac{\partial T_0}{\partial x}, \quad (10b)$$

$$\nabla^2 \psi_0 = -\omega_0. \quad (10c)$$

Each of the derivatives are discretized by a second-order centered difference scheme and each of the (T_n, ω_n, ψ_n) terms are computed by solving a discrete Poisson equation with Dirichlet boundary conditions. Due to the sparsity of the resultant matrices, the method was implemented in $\mathcal{O}(N \log N)$ operations where N is the total number of points in the discretization. A key result of this iteration is that it only converges within a parameter regime that corresponds to a small St number. In practice, this implies that the solver above is ineffective for large laser irradiance and absorption values; the exact threshold for convergence depends on the other flow parameters and domain

size. Figure 1(a) demonstrates the relationship between the numerical domain size (D) and the threshold for convergence manifested through the St number. We observe that the largest convergent St number decreases with third-order dependence on the domain size. In Section 3 we provide examples of parameter regimes in which the method fails to converge, with implications for the performance of the simulation as a

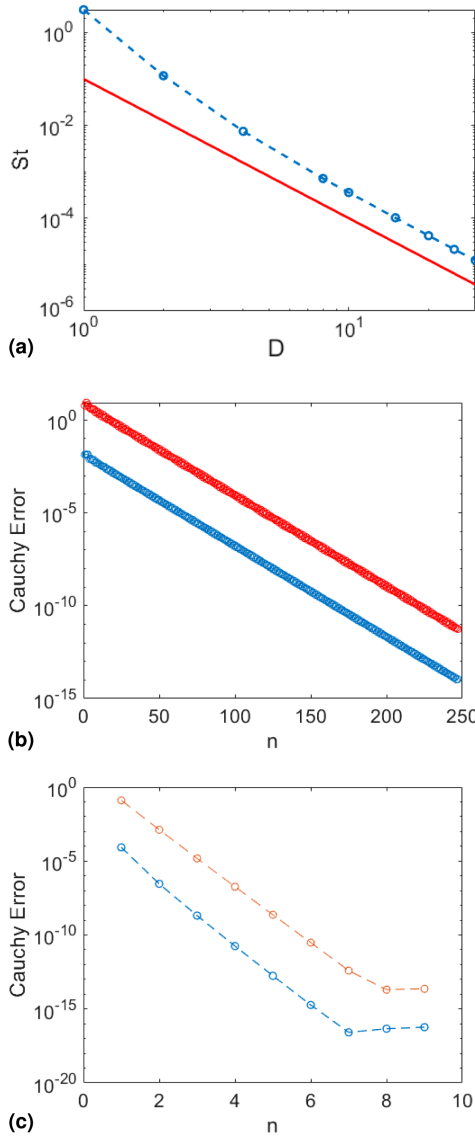


Fig. 1. (a) The largest St number within the convergence region of the fluid solver is presented as a function of the scaled domain length (D) as the dotted blue line. All other parameters are fixed. The convergent St numbers tend toward third-order scaling as a function of increased computational domain size, depicted with the solid red line. (b) The Cauchy error for temperature (blue) and vorticity (red) is depicted in the fixed-point fluid solver. For a total number of domain points N , the iteration converges linearly and has a computational cost of $\mathcal{O}(N \log(N))$. This iteration thus offers a faster alternative to Newton’s method for large problems, which converges quadratically but has a higher cost per iteration. (c) The Cauchy error for temperature (blue) and laser amplitude (red) is depicted in the iteration for laser evolution. The error exhibits a linear convergence rate until reaching machine precision, at which point the algorithm terminates.

whole. Figure 1(b) depicts the linear convergence rate of the temperature and vorticity in the fixed-point algorithm.

2. Laser Evolution

The paraxial equation Eq. (5) was used as the model for the beam propagation. We used the method of Akers and Reeger [4], which approximates the volumetric fluid via linear interpolation between 2D slices. We placed these slices at discrete locations along the propagation path, with a constant distance between slices of Δz that results in $\mathcal{O}(\Delta z^2)$ accuracy from the paraxial scaling. The Fourier collocation method and sixth-order Runge–Kutta method were used to discretize derivatives and evolve the paraxial equation in z .

Since the fluid solver in Eqs. (9) and (12) requires a known laser irradiance profile, however, we could not directly solve for the steady state on consecutive fluid slices. Instead, we applied an iteration that proceeds by successively firing the laser until the fluid response between consecutive slices is unchanged. Here are the basic steps of this procedure:

Let T^k and V^k be the temperature and laser amplitude at the k th fluid slice, noting that the k index is a superscript and not an exponent. Next, introduce a sequence of guesses for the temperature $\{\mathcal{T}_n\}$ and the amplitude $\{\mathcal{V}_n\}$ at the next slice, initialized by

$$\mathcal{T}_0 = T^k, \quad \mathcal{V}_0 = V^k. \tag{11}$$

These iterative variables are then evolved by implementing the paraxial and fluid solvers, where $T^*(\mathcal{V})$ is the temperature fixed-point solution to the fluid equations for an amplitude \mathcal{V} and $V^*(\mathcal{T}_i, \mathcal{T}_j)$ is the numerical solution to the paraxial equation between two slices with temperatures \mathcal{T}_i and \mathcal{T}_j , respectively. The iteration proceeds as

$$\mathcal{V}_{n+1} = V^*(\mathcal{T}^k, \mathcal{T}_n), \tag{12a}$$

$$\mathcal{T}_{n+1} = T^*(\mathcal{V}_{n+1}). \tag{12b}$$

Convergence is achieved when the fluid response and laser amplitude stop changing within the iteration. Therefore, when the Cauchy error in temperature drops below the numerical threshold for convergence δ_T after some step number \mathcal{N} , then

$$\|\mathcal{T}_{\mathcal{N}} - \mathcal{T}_{\mathcal{N}-1}\|_2 < \delta_T, \tag{13}$$

and the iteration terminates. The fluid temperature and laser amplitude at the $(k + 1)$ th slice are then updated as

$$T^{k+1} = \mathcal{T}_{\mathcal{N}}, \quad V^{k+1} = \mathcal{V}_{\mathcal{N}}. \tag{14}$$

All simulations in the following section are performed with $\delta_T = 10^{-15}$ and $\Delta z = 10$ cm. Figure 1(c) depicts the convergence of fluid temperature and laser amplitude between the aperture and the first slice of the laser evolution iteration.

3. SIMULATION RESULTS

This section provides several realizations of the coupled Boussinesq-paraxial solver to showcase thermal blooming as a function of different laser-fluid parameters. The parameters of interest are the laser absorption coefficient β , the extinction

coefficient α , the propagation distance L_z , the length of one side of the square computational domain D , the wavenumber k , and the peak aperture irradiance V_0^2 . Each of the other parameters in the simulation were taken to be constant and corresponded to the standard laboratory conditions from the experiment in steady-state thermal blooming from Cook *et al.* [31]. These values are: $\tau_0 = 300$ K, $\nu = 0.15$ cm²/s, $\mu = 0.2$ cm²/s, $L_x = 0.5$ cm, $n_0 = 1.0003$, and $g = 981$ cm/s². The length scale L_x corresponds to the Gaussian beam radius, and the velocity scale U is reported *a posteriori* as the convective velocity at the center of the domain. Since the degree of convection (and thus U) depends on parameters such as laser absorption and peak irradiance, we reported the value of each of the nondimensional parameters based on the simulation results. By taking this approach, we ensured each parameter retained its physical meaning so the flow characteristics can be interpreted from these parameters. Note in this analysis that the steady-state solution is very sensitive to the global boundary conditions and domain size—simulation parameters whose impact is often neglected in time-dependent simulations. Therefore, it is important to think carefully about what the domain should look like in a steady problem; especially when attempting to simulate atmospheric propagation with no obvious boundaries. The no-friction slip condition used in this simulation effectively imposed a finite box as the boundary, meaning that these simulation results should be understood in this context. In the steady problem, locally heated flow convected from the center approached the boundary and recirculated in the domain until a steady-state was reached. Thus, the localized heating effect results in global changes to the steady-state flow as a function of the boundary conditions and domain size. This differs from time-dependent thermal blooming since the boundary of a sufficiently large domain has no localized effect on the flow for the short time scales used in [4]. Lane and Akers are currently investigating how the steady-state precisely depends on the domain, and we seek to develop open boundary conditions for the steady-state problem based on insights from time-dependent simulations.

As a basis for comparison to the aforementioned thermal blooming experiment [31], the first simulation we considered had a small domain with length $D = 2.5$ cm such that $\Omega = [-1.25, 1.25] \times [-1.25, 1.25]$ cm and the laser propagated a distance of $L_z = 5.3$ m. The experimental laser wavelength was tuned to align with the peak water absorption bands, so the extinction and absorption parameters were large due primarily to the water absorption within the fluid. The numerical domain size must be large enough to contain the fully bloomed irradiance profile, but it also must be small enough to allow for fluid equation convergence at high absorption values. The laser wavelength was 1944.907 nm, which corresponds to a wavenumber of 3.2306×10^4 cm⁻¹, and the Gaussian beam had a power of 5 W, which corresponds to a peak aperture irradiance of $V_0^2 = 12.7$ W/cm². The extinction was $\alpha = 5.25 \times 10^{-4}$ cm⁻¹, and the laser absorption coefficient was $\beta = 4.26 \times 10^{-5}$ m² K/J, where we assumed no aerosol presence to contribute to scattering losses. Figure 2 depicts the simulated temperature fluctuation and laser irradiance along the propagation path.

Along the longitudinal path in Fig. 2, we observed that the steady temperature fluctuation bloomed out from the center

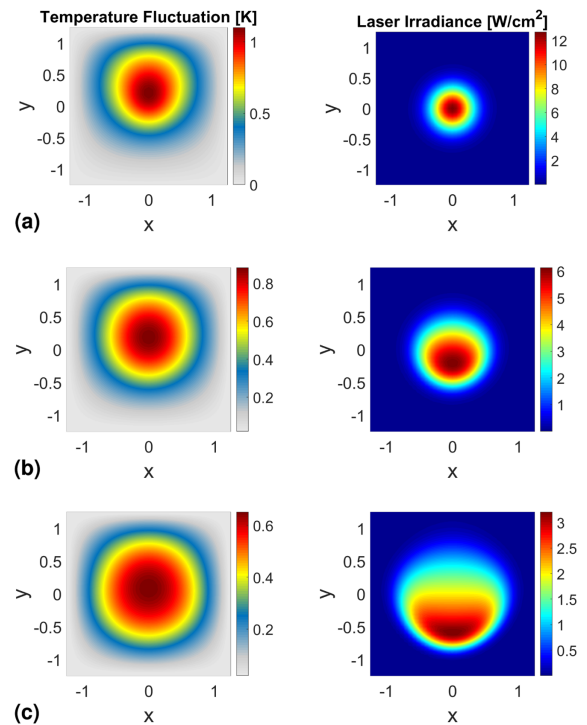


Fig. 2. Left column gives the simulated temperature fluctuations in degrees K for $z = 0$ (top), $z = 3$ m (middle), and $z = 5.3$ m (bottom). The domain size is $D = 2.5$ cm and the peak aperture irradiance is 12.7 W/cm². The right column gives the simulated laser irradiance in W/cm² for $z = 0$ (top), $z = 3$ m (middle), and $z = 5.3$ m (bottom). The laser wavenumber is 3.2306×10^4 cm⁻¹ and the convective velocity scale is $U = 0.56$ cm/s. The nondimensional fluid parameters are $Re = 1.9$, $Pe = 1.4$, $Ri = 1564$, and $St = 1/125$. (a) Temperature fluctuation (left) and laser irradiance (right) at the aperture. (b) Propagation after $z = 3$ m. (c) Propagation after $z = 5.3$ m.

and became more radially symmetric. The irradiance profile spreads out from the original spot size and exhibited a standard half-moon shape seen in other steady thermal blooming studies [5,37]. The formation of a half-moon shape toward the bottom of the domain was indicative of strong thermal blooming, wherein the beam experiences beam spreading and beam wander. The shift in index of refraction induced by the temperature fluctuations led to the shift downward and into the half-moon pattern observed in the simulation at the target location of

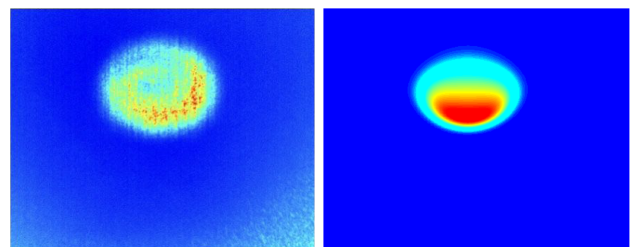


Fig. 3. Left image gives the experimental thermal blooming profile and the right image gives the simulated thermal blooming profile for a laser wavenumber of 3.2306×10^4 cm⁻¹. The domains are scaled to the same size of 5.6×5.8 cm and the beam propagates over a distance of 5.3 m. The nondimensional parameters are the same as in Fig. 2; namely, $Re = 1.9$, $Pe = 1.4$, $Ri = 1564$, and $St = 1/125$.

$z = 5.3\text{m}$. The beam blooms outwards to approximately 1 cm in width, doubling its original spot size. This blooming profile was achieved without the imposition of any crosswind, which showcased the sufficiency of natural convection to induce temperature fluctuations at the degree needed for strong thermal blooming.

Figure 3 provides a comparison of the simulation to the experiment at an equivalent wavelength of 1944.907 nm. The experimental blooming profile was captured as part of the same experiments contained in Cook *et al.* [31]. The experiment was performed within a 5.3 m long climate-controlled chamber at standard temperature and pressure. The air was quiescent at the time of firing and the images were captured after the time-dependent beam dynamics settled into an observed steady state. A wavemeter was used to measure and validate the laser wavelength and a FLIR camera was positioned to image the beam irradiance at the end of the propagation chamber.

For applications related to atmospheric laser propagation, the laser wavelength is often chosen to fall within an atmospheric transmission window with very low molecular absorption values. In these transmission windows, the extinction coefficient is composed almost entirely from scattering due to aerosol presence [11,29]. At a wavelength of 1.045 μm , for example, the laser absorption coefficient can be as low as $\beta = 10^{-9} \text{ m}^2 \text{ K/J}$

with an extinction coefficient of $\alpha_f = 10^{-3} \text{ km}^{-1}$ without aerosols and $\alpha_a = 0.32 \text{ km}^{-1}$ with aerosol scattering. Since the laser absorption coefficient is significantly reduced relative to the values in the experiment, the St number is equivalently reduced for the same laser irradiance value. Therefore, within this transmission window, the simulation can account for much higher laser powers. Since many studies in thermal blooming are devoted to high energy lasers, this parameter regime provides the best basis of comparison for atmospheric propagation. We note that the simulation is not suitable to simulate propagation over distances that are on the order of kilometers or longer; the required domain size becomes too large to permit convergence in the fixed-point fluid solver. We are actively researching the extension of the fluid solver to larger domains through analytic continuation and functional approximation methods.

Figure 4 depicts the simulated temperature fluctuation and laser irradiance for a 43.2 kW/cm² laser with a wavelength of 1.045 μm . The absorption and extinction coefficients coincide with the transmission window above and include aerosol scattering effects. The domain is $\Omega = [-2, 2] \times [-2, 2]$ cm to demonstrate blooming at a target distance of $L_z = 20 \text{ m}$.

In this regime, we observed the formation of a pronounced crescent shape at the target. Along the propagation path, the

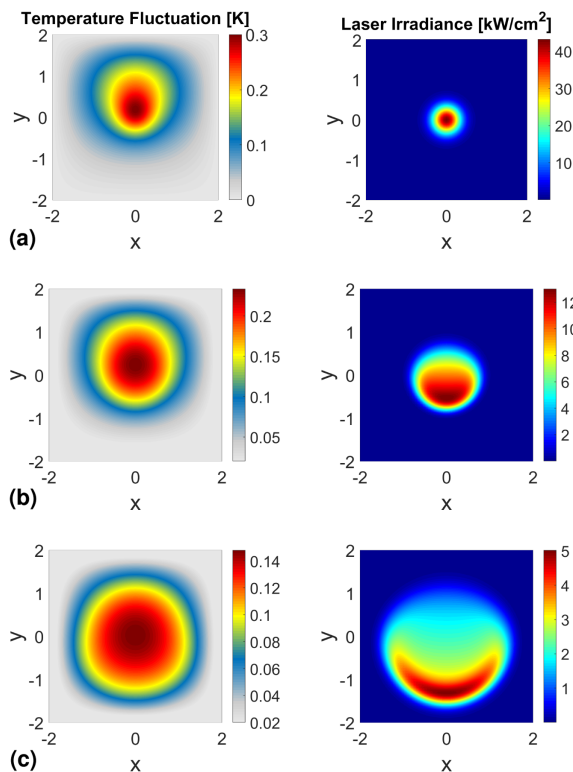


Fig. 4. Left column gives the simulated temperature fluctuations in degrees K for $z = 0$ (top), $z = 10 \text{ m}$ (middle), and $z = 20 \text{ m}$ (bottom). The domain size is $D = 4 \text{ cm}$ and the peak aperture irradiance is 43.2 kW/cm^2 . The right column gives the simulated laser irradiance in kW/cm² at the same distances. The laser wavenumber is $k = 6.0126 \times 10^4 \text{ cm}^{-1}$ and the convective velocity scale is $U = 0.3 \text{ cm/s}$. The nondimensional parameters are $\text{Re} = 1.0$, $\text{Pe} = 0.75$, $\text{Ri} = 5450$, and $\text{St} = 1/419$. (a) Temperature fluctuation (left) and laser irradiance (right) at the aperture. (b) Propagation after $z = 10 \text{ m}$. (c) Propagation after $z = 20 \text{ m}$.

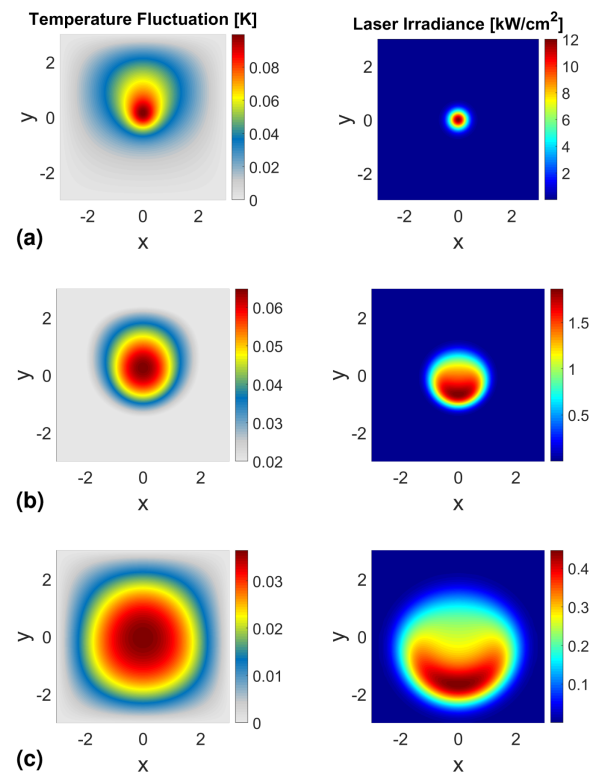


Fig. 5. Left column gives the simulated temperature fluctuations in degrees K for $z = 0$ (top), $z = 25 \text{ m}$ (middle), and $z = 50 \text{ m}$ (bottom). The domain size is $D = 6 \text{ cm}$ and the peak aperture irradiance is 12 kW/cm^2 . The right column gives the simulated laser irradiance in kW/cm² at the same distances. The laser wavenumber is $k = 6.0126 \times 10^4 \text{ cm}^{-1}$ and the convective velocity scale is $U = 0.225 \text{ cm/s}$. The nondimensional parameters are $\text{Re} = 0.75$, $\text{Pe} = 0.56$, $\text{Ri} = 9689$, and $\text{St} = 1/1125$. (a) Temperature fluctuation (left) and laser irradiance (right) at the aperture. (b) Propagation after $z = 25 \text{ m}$. (c) Propagation after $z = 50 \text{ m}$.

laser wavefront progressively bloomed outward from a half-moon to a strong crescent shape while exhibiting beam bending toward the bottom of the domain. As the beam spot underwent thermal blooming, the points on the crescent became sharper before approaching the edge of the numerical domain. To simulate blooming at longer propagation distances, the numerical domain size must increase. In doing so, however, the range of St numbers for which the fixed-point solver converges decreases. Thus, there is a trade-off between the laser energy and the propagation distance in the simulation since a smaller power laser permits a larger numerical domain. Again, we are pursuing efforts to improve the fluid solver to account for larger St numbers given a specific domain size. As an example of thermal blooming at a longer propagation distance, Fig. 5 provides the simulated temperature fluctuation and laser irradiance for a 12 kW/cm^2 laser at a propagation distance of $L_z = 50 \text{ m}$ with the same wavelength, absorption, and extinction parameters in the previous simulation. The domain was increased in size to $\Omega = [-3, 3] \times [-3, 3] \text{ cm}$ to allow for an increased beam spread at the longer distance, which required a smaller laser power than was simulated in Fig. 4. The beam irradiance profiles without thermal blooming are given as a reference in Fig. 6 for 5.3, 20, and 50 m propagation distances.

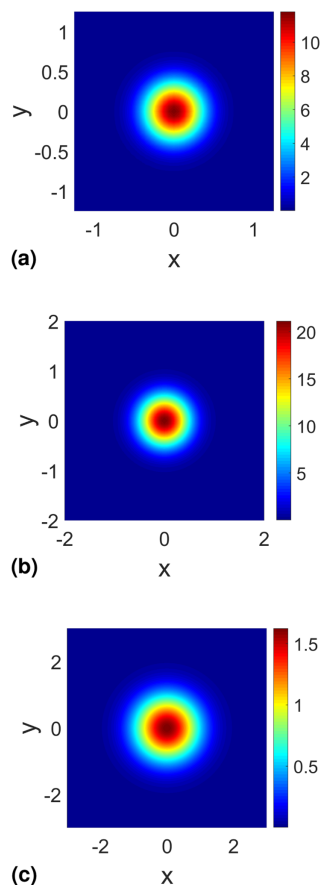


Fig. 6. (a) Laser irradiance after 5.3 m propagation with no fluid interaction. The domain size and laser power are the same as in Fig. 2. (b) Laser irradiance after 20 m propagation with no fluid interaction. The domain size and laser power are the same as in Fig. 4. (c) Laser irradiance after 50 m propagation with no fluid interaction. The domain size and laser power are the same as in Fig. 5.

4. CONCLUSIONS

This work investigated steady-state laser propagation through the direct numerical simulation of laser-induced natural convection. The numerical simulation solves the steady, 2D Navier–Stokes equations in a buoyancy-driven flow regime coupled to the paraxial equation for laser propagation. The simulation is fast through the use of sparse finite difference solvers with computational cost $\mathcal{O}(N \log(N))$, and the numerical method to couple the flow to the beam evolution is, to the best of our knowledge, novel. Steady-state convective thermal blooming studies were conducted in three parameter regimes. While the numerical method was fast, it was limited to a small St number. Simulating thermal blooming over longer propagation distances requires a larger numerical domain, which reduces the range of St numbers that can be simulated. Within this parameter range, however, the presented method is able to simulate fully resolved crescent patterns in the laser irradiance. Future research efforts are underway that seek to improve the performance of the steady fluid solver with respect to convergent parameter regimes using mathematical methods such as numerical and analytic continuation. A related research problem currently in progress is to determine the optimal boundary conditions and domain size for an atmospheric propagation simulation with no obvious physical boundaries.

Funding. Air Force Office of Scientific Research.

Acknowledgment. The authors thank Dr. Steven Fiorino of the Air Force Institute of Technology for comments on the aerosol contribution to thermal blooming. This report was prepared as an account of work sponsored by an agency of the United States government. Neither the United States government nor any agency thereof, nor any of their employees, make any warranty, express or implied, or assume any legal liability or responsibility for the accuracy, completeness, or usefulness of any information, apparatus, product, or process disclosed, or represents that its use would not infringe privately owned rights. Reference here to any specific commercial product, process, or service by trade name, trademark, manufacturer, or otherwise does not necessarily constitute or imply its endorsement, recommendation, or favoring by the United States government or any agency thereof. The views and opinions of authors expressed here do not necessarily state or reflect those of the United States government or any agency thereof.

Disclosures. The authors declare no conflicts of interest.

Data availability. No data were generated or analyzed in the presented research.

REFERENCES

1. F. G. Gebhardt, "High power laser propagation," *Appl. Opt.* **15**, 1479–1493 (1976).
2. D. C. Smith, "High-power laser propagation: thermal blooming," *Proc. IEEE* **65**, 1679–1714 (1977).
3. N. R. Van Zandt, S. T. Fiorino, and K. J. Keefer, "Enhanced, fast-running scaling law model of thermal blooming and turbulence effects on high energy laser propagation," *Opt. Express* **21**, 14789–14798 (2013).
4. B. F. Akers and J. A. Reeger, "Numerical simulation of thermal blooming with laser-induced convection," *J. Electromagn. Waves Appl.* **33**, 96–106 (2019).
5. S. Reich, S. Schäffer, M. Lueck, M. Wickert, and J. Osterholz, "Continuous wave high-power laser propagation in water is affected by strong thermal lensing and thermal blooming already at short distances," *Sci. Rep.* **11**, 22619 (2021).
6. M. H. Mahdiah, "Two-dimensional-simulation of thermal blooming effects in ring pattern laser beams," *Opt. Eng.* **44**, 096001 (2005).

7. M. F. Spencer, "Wave-optics investigation of turbulence thermal blooming interaction: I. Using steady-state simulations," *Opt. Eng.* **59**, 081804 (2020).
8. M. F. Spencer, "Wave-optics investigation of turbulence thermal blooming interaction: II. Using time-dependent simulations," *Opt. Eng.* **59**, 081805 (2020).
9. M. Lax, W. Louisell, and W. McKnight, "From Maxwell to paraxial wave optics," *Phys. Rev. A* **11**, 1365 (1975).
10. R. Z. Yahel, "Turbulence effects on high energy laser beam propagation in the atmosphere," *Appl. Opt.* **29**, 3088–3095 (1990).
11. P. Sprangle, J. R. Peñano, A. Ting, and B. Hafizi, "Propagation of high-energy lasers in a maritime atmosphere," NRL Review ADA471880 (Naval Research Lab, 2004), pp. 59–65.
12. M. F. Spencer, I. V. Dragulin, D. S. Cargill, and M. J. Steinbock, "Digital holography wave-front sensing in the presence of strong atmospheric turbulence and thermal blooming," *Proc. SPIE* **9617**, 961705 (2015).
13. M. F. Spencer and S. J. Cusumano, "Impact of branch points in adaptive optics compensation of thermal blooming and turbulence," *Proc. SPIE* **8165**, 816503 (2011).
14. J. E. Pearson, "Thermal blooming compensation with adaptive optics," *Opt. Lett.* **2**, 7–9 (1978).
15. P. S. Salter and M. J. Booth, "Adaptive optics in laser processing," *Light Sci. Appl.* **8**, 110 (2019).
16. J. Hecht, "Short history of laser development," *Opt. Eng.* **49**, 091002 (2010).
17. G. P. Perram, M. A. Marciniak, and M. Goda, "High energy laser weapons: technology overview," *Proc. SPIE* **5414**, 1–25 (2004).
18. D. L. Carroll, "Overview of high energy lasers: Past, present, and future?" in *42nd AIAA Plasmadynamics and Lasers Conference* (2011), pp. 1–21.
19. J. Kasparian, L. Wöste, and J.-P. Wolf, "Laser-based weather control," *Opt. Photon. News* **21**(7), 22–27 (2010).
20. S. H. Kim, S. R. Choi, and D. Kim, "Thermal conductivity of metal-oxide nanofluids: particle size dependence and effect of laser irradiation," *J. Heat Transfer* **129**, 298–307 (2007).
21. A. M. Salman, A. A. Salman, and A. Al-Janabi, "Stable L-band multiwavelength erbium-doped fiber laser based on four-wave mixing using nickel nanofluid," *Appl. Opt.* **58**, 6136–6143 (2019).
22. E. Vela, M. Hafez, and S. Régner, "Laser-induced thermocapillary convection for mesoscale manipulation," *Int. J. Optomech.* **3**, 289–302 (2009).
23. E. Flores-Flores, S. A. Torres-Hurtado, R. Páez, U. Ruiz, G. Beltrán-Pérez, S. L. Neale, J. C. Ramírez-San-Juan, and R. Ramos-García, "Trapping and manipulation of microparticles using laser-induced convection currents and photophoresis," *Biomed. Opt. Express* **6**, 4079–4087 (2015).
24. V. Coffey, "New advances in defense applications: high-energy lasers," *Opt. Photon. News* **25**(10), 28–35 (2014).
25. R. M. Rennie, E. J. Jumper, and E. C. Marineau, "Investigation of the importance of convective heat transfer on laser-induced heating," *J. Thermophys. Heat Transfer* **24**, 573–580 (2010).
26. T. J. Nugent, Jr. and J. T. Kare, "Laser power beaming for defense and security applications," *Proc. SPIE* **8045**, 804514 (2011).
27. C. H. Chan, "Effective absorption for thermal blooming due to aerosols," *Appl. Phys. Lett.* **26**, 628–630 (1975).
28. P. Sprangle, J. Peñano, and B. Hafizi, "Optimum wavelength and power for efficient laser propagation in various atmospheric environments," *J. Dir. Energy* **2**, 71–95 (2006).
29. S. T. Fiorino, R. J. Bartell, M. J. Krizo, G. L. Caylor, K. P. Moore, T. R. Harris, and S. J. Cusumano, "A first principles atmospheric propagation and characterization tool: the laser environmental effects definition and reference (LEEDR)," *Proc. SPIE* **6878**, 68780B (2008).
30. J. S. Lane and B. F. Akers, "Two-dimensional steady Boussinesq convection: existence, computation and scaling," *Fluids* **6**, 425 (2021).
31. J. Cook, P. Roumayah, D. J. Shin, J. Thompson, A. Sincore, N. Vail, N. Bodnar, and M. Richardson, "Narrow linewidth 80 W tunable thulium-doped fiber laser," *Opt. Laser Technol.* **146**, 107568 (2022).
32. D. Acheson, *Elementary Fluid Dynamics* (Oxford University, 1990).
33. L. Landau and E. M. Lifshitz, *Fluid Mechanics*, 2nd ed., Vol. **6** of Course of Theoretical Physics (Pergamon, 1987).
34. L. Quartapelle, *Numerical Solution of the Incompressible Navier-Stokes Equations*, 1st ed. (Birkhauser Verlag, 1993).
35. P. M. Gresho and R. L. Sani, "On pressure boundary conditions for the incompressible Navier-Stokes equations," *Int. J. Numer. Methods Fluids* **7**, 1111–1145 (1987).
36. C. Hogge, "Propagation of high-energy laser beam in the atmosphere," Tech. Rep. AD0781763 (Air Force Weapons Laboratory, 1974).
37. L. Zhao, J. Wang, M. Guo, X. Xu, X. Qian, W. Zhu, and J. Li, "Steady-state thermal blooming effect of vortex beam propagation through the atmosphere," *Opt. Laser Technol.* **139**, 106982 (2021).